Examining the high-pressure response and shock melting in cerium using optical pyrometry

B. J. Jensen,[*] T. M. Hartsfield, D. B. Holtkamp,[†] and F. J. Cherne
Los Alamos National Laboratory, Los Alamos, New Mexico 87545, USA

R. B. Corrow, T. E. Graves, and A. J. Iverson[†]
Nevada National Security Site, New Mexico Operations, Los Alamos, New Mexico 87544, USA

The ability to measure temperature in shock wave experiments has been a long-standing scientific challenge complicated by the short timescales involved (<1 microsecond) and the presence of nonthermal or external light sources that pollute measured radiances using optical pyrometry methods. In the current work, we present the first experimental data on cerium metal designed to measure the temperature on-Hugoniot from the low-pressure α phase well into the high-pressure liquid phase. Radiance data obtained in this work were used to determine the Hugoniot curves for solid (α-Ce) and liquid cerium by measuring the longitudinal stress and temperature simultaneously in the shocked state. These data were used to estimate the temperature for incipient shock melting and complete melting, and to further constrain a multiphase equation of state developed to describe the dynamic response of cerium at high pressures.

I. INTRODUCTION

The ability to measure the temperature of shocked metals remains a long-standing scientific challenge. Traditional shock wave diagnostics provide information on the mechanical state of the material (i.e., stress, density, internal energy) whereas temperatures are typically calculated using the governing equations coupled with an assumed equation of state [1]. This has led to controversies that remain today between melt temperatures of metals at high pressures obtained using diamond anvil cell (DAC) and dynamic-compression experiments [2–5]. In the last decade, significant developments in using optical pyrometry applied to shock wave experiments are providing new opportunities to measure temperature in shocked metals [6–8]. Accurate temperature measurements are required to generate well-constrained and experimentally validated equation-of-state (EOS) models to describe the response of matter-at-extremes which are relevant to many fields including condensed matter physics, solid and fluid mechanics, and planetary science.

Optical pyrometry [9] is currently the best-developed, general-purpose method for measuring dynamic temperatures in opaque shocked materials. It has been employed to study temperature states of shocked metals for decades with varying results [10–12]. Optical pyrometry attempts to deduce temperature from careful measurement at known wavelengths (radiometry) of the calibrated quantity of spectral radiance emitted by a surface at finite temperature [13–17]. Temperature calculation via the Planck function then requires assumptions about the spectral emissivity of the emitting surface under compression. For equation-of-state measurements, the sample material is generally held in compression by contact with an optically transparent anvil window to permit measurement of high-pressure states and to simplify the nature and emissivity of the emitting surface [18,19]. Beyond the lack of knowledge of exact spectral emissivity under shock loading, dynamic phenomena such as shock release of the anvil window, flashes from gun or HE drive systems, gas compression from flyer impacts, and conditional optical emission from shock reverberation of sample-window bond layers can easily contaminate radiance measurements. These highly energetic phenomena and short timescales, less than 1 μs associated with dynamic-compression experiments, make reliable temperature measurements elusive. Recent developments have coupled optical pyrometry with simultaneous reflectance measurements using integrating spheres to obtain radiance and emissivity, significantly reducing the uncertainty in temperature estimates and accounting for changes in the sample surface during dynamic loading [6–8].

Cerium metal has received significant attention over the years because of its complex phase diagram as shown in Fig. 1. Diamond anvil cell data reveal multiple solid-solid phases at high pressure [20–23], three at zero pressure, and an anomalous melt boundary with a broad minimum at approximately at 3.3 GPa and 933 K [24,25]. At low pressures, cerium transforms isostructurally from the γ phase (fcc) to the α phase (fcc) at 0.75 GPa [22,26,27] accompanied by a large volume collapse of 13–16 percent. Continuing along a room-temperature isotherm, cerium is known to transform to the ϵ phase (bct) above 13 GPa [28]. At higher temperatures this transition is more uncertain with multiple boundaries reported [20,21]. During shock loading, this large volume collapse at the γ-α boundary leads to a significant rise in temperature resulting in a shock-melt transition near
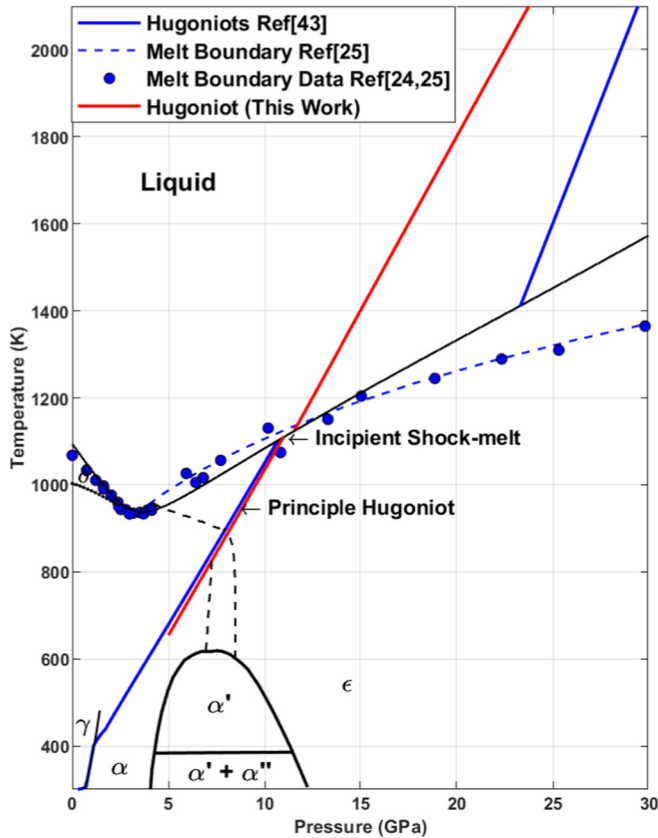
FIG. 1. Schematic of the phase diagram for Ce. The Hugoniot (blue line) and the melt boundary (solid black curve) obtained from a published EOS [43]. Blue-filled circles represent DAC data for the melt boundary [24,25]. Dashed black lines represent two of the reported boundaries for the α-ϵ region of the phase diagram. The solid red line indicates the Hugoniot developed in this work based on measurements of temperature and stress.

10–11 GPa [29] significantly lower than many metals. Early shock compression experiments [1] estimate a melt temperature near 3700 K inconsistent with extrapolated diamond anvil cell data that suggest a significantly lower melt temperature of 1515 K [25]. In this work, experiments were performed using optical pyrometry and interface velocimetry to simultaneously measure the temperature and longitudinal stress for cerium shocked to stress states that span the shock-melt transition. These data were used to determine the Hugoniot (T, P) for solid α-Ce and liquid Ce, to estimate the temperature for incipient and complete melting, and to constrain an existing multiphase equation of state (EOS) for cerium. Experimental methods and results are presented in Secs. II and III, respectively. Data analysis and discussion are presented in Sec. IV, followed by the conclusions in Sec. V and our acknowledgments.

II. EXPERIMENTAL METHODS

Shock waves were generated in the cerium samples through plate impact using single- and two-stage gas guns capable of reaching velocities up to 3 km/s. The experiment configuration is shown in Fig. 2 and consisted of a metal flyer
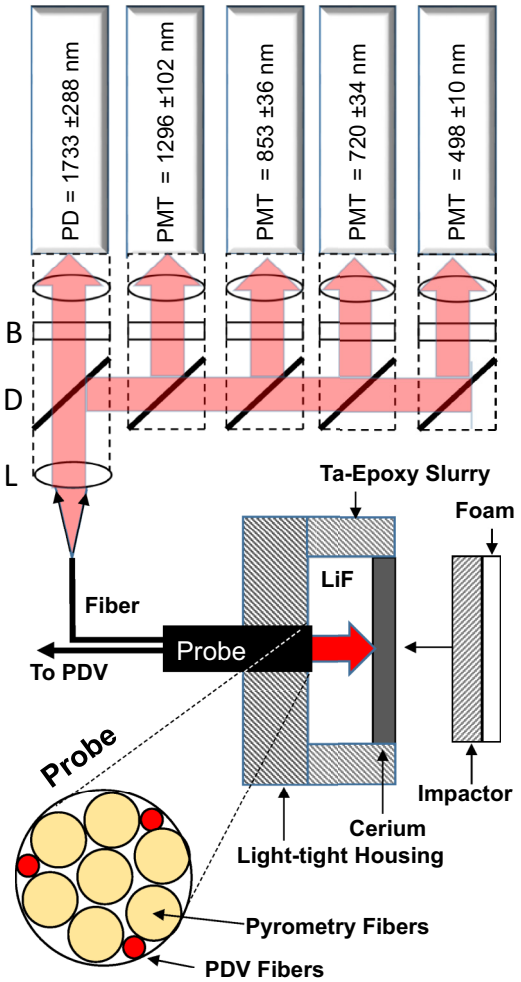

FIG. 2. Schematic of the experimental configuration for temperature measurements on shocked cerium. The target and projectile configuration consisted of a foam-backed impactor, cerium sample, and LiF window. The dual PDV-radiance probe is indicated along with a close-up that illustrates the optical fiber packing pattern. The pyrometer configuration shows that light collected from the Ce-LiF interface is coupled to the five-channel pyrometer. The system collimates broadband optical and near-infrared signal light out of the input fiber through a lens element (L) and passes the beam through a series of increasing-wavelength dichroic beam splitters (D). The spectrally selected beams, further filtered through an optical band-pass filter (B) centered around each given wavelength, are focused onto the detector photosensitive areas by further lensing.

plate (1-inch diameter) backed by syntactic foam impacting a cerium sample (2-inch diameter $\times$ 1–2 mm thick). A LiF optical window (2-inch diameter $\times$ 19 mm thick) was used to maintain the particle velocity or stress state at the Ce-LiF interface during the experiment. A shock wave generated at impact reflects from the Ce-LiF creating a steady compressed state with a duration (>300 nanoseconds) bounded by arrival of release waves from the back of the impactor and the LiF window. Photonic Doppler velocimetry (PDV) [30–32] was used to measure the particle velocity of the Ce-LiF interface to characterize the stress states during the experiment. A simultaneous measurement of the light radiating from the cerium sample provided a measure of the shocked

temperature. Projectile velocities were measured using a series of optical beam interrupts with accuracies on the order of 0.1%–0.2% [31]. LiF optical windows obtained from Reflex Analytical were used for all experiments due to the close impedance match to Ce coupled with their well-known optical and shock wave properties [31,33]. High-purity cerium samples (99.99%) similar to those used in past work [29] were used for all experiments.

Temperatures were calculated from thermal radiance accurately measured from the Ce surface using a multichannel optical pyrometer shown schematically in Fig. 2. The system collects thermal radiation from a small spot in the center of the target surface via a focusing probe optical assembly with lenses that refocus that light onto a close-packed fiber bundle. The bundle contains seven 300-micron (0.28 NA) core low-OH silica fibers to collect thermal radiance and three single-mode fibers (0.14 NA; 9-micron core) used to couple 1550 nm wavelength laser light for the PDV measurement. Dichroic mirrors and bandpass filter elements create five optical channels, in the visible and near-IR spectrum, each measured by a single photomultiplier tube (PMT) or photodiode detector. Note that the InSb photodiode has greater sensitivity to the longer wavelengths than the PMT, but with a slower response time (10 MHz, vs 300 MHz for the PMT) so that rise time of the detector is approximately 80 ns. Capturing the very high dynamic range of the photomultiplier tubes requires multiple digitizer coverages; each detector was monitored by three to five digitizer channels, set to measure signal levels from less than a millivolt up to tens of volts. To calibrate the pyrometer, a linear voltage-vs-radiance function was assembled for each channel. The pyrometry probe was aligned to collect thermal radiation from a portable blackbody standard (Mikron Infrared, Inc., model M330; Infrared Systems Development Corp., model IR-564). Light from the back of the cavity was focused onto the probe, overfilling its field of view. Thermal radiation collected through the probe passes through the fiber bundle and then through an optical chopper and a shutter to create isolated pulses of 100 microsecond duration. For each channel, the detector voltage during the peak of this pulse was averaged over time and the corresponding radiance of the channel was calculated from a spectral multiplication of the Planck spectrum at the temperature of the calibration standard and the measured spectral response of the bandpass filter.

The LiF optical windows produce a steady stress state at the Ce-LiF interface and maintain the nearly uniform field of view required for the optical pyrometry measurements. LiF was used as a window because it was found to remain transparent during shock loading, and thus does not emit its own thermal light for shocked stress states up to approximately 160 GPa. However, studies have shown [34] that when the shock wave releases from the edge of the window a significant amount of nonthermal, spectrally varying light is generated (likely caused by fracture) that pollutes the light collected from the cerium sample. This LiF edge-release light was mitigated by surrounding the Ce-LiF target with a Ta-vinyl slurry to match shock impedance with the LiF, or by utilizing undersized impactors to delay edge release. Extraordinary care was taken to prevent contamination of black-body photons from the metal surface by external sources of light such as the impact flash caused by the projectile compressing gas in front of the target. The LiF windows used opaque metallic edge coatings and the edges and gaps in the target fixtures were covered with black paint. The LiF windows were bonded to the Ce using Loctite 326 epoxy, which was found not to emit light during shock loading for the entire stress range achieved in this study. The glue layer also acts as a thermal barrier, preventing cooling of the Ce sample surface to temperatures substantially below the bulk Ce material temperature [35].

Calculating pyrometric temperature requires knowledge of both spectral radiance and spectral emissivity. In these experiments, we could not control or measure the spectral reflectivity of the cerium surfaces because rapid oxidation transforms the surface of bare Ce. Even when epoxy-bonded to a LiF window, we observed reflectivity variations across single surfaces as well as variations from sample to sample. Furthermore, it is not known how the emissivity changes during shock loading, and in particular, during phase transitions including the shock-melt transition accessed in these experiments. Determining temperature from radiance data with an unknown emissivity which varies with wavelength is an ill-posed problem. Traditionally, researchers have assumed either a "gray-body" hypothesis ($\epsilon_1 = \epsilon_2$, etc.) or a functional form for the emissivity $\epsilon = f(\lambda)$ [9]. An alternative approach [36,37] was to perform radiance measurements at multiple wavelengths (specifically the bluest practical wavelengths) and combine these N measurements of radiance with $2N$ constraints (an upper and lower bound on the allowed dynamic emissivity at each channel wavelength). This produces N values for T with an associated ΔT for the allowed range of ϵ. Our analysis assumes a spectral emissivity between 0.3 and 0.8, varying by channel, based on published (n, k) values [38], known observations, and recent experiments which have shown generally modest changes in spectral emissivity under dynamic loading [6–8]. Our system was designed to measure the shortest possible wavelengths, where the uncertainty in temperature due to uncertainty in spectral emissivity is minimized [16].

III. EXPERIMENTAL RESULTS

A total of 17 experiments were performed in this work with impact stresses designed to span the high-pressure solid phase (α-Ce) and well into the liquid phase. The relevant experimental parameters and measured/calculated quantities are shown in Table I. The measured particle velocity at the cerium-LiF interface is shown in column 6 along with the longitudinal stress calculated from known shock response of LiF in column 7. Temperature values calculated from the radiance profiles are shown in column 8. The Hugoniot stress state (column 9) was obtained using both standard impedance-matching methods [39] that used the measured particle velocity (column 6) and calculations using a one-dimensional hydrocode with material descriptions for 6061-T6 Al, OFHC Cu, Ta, and LiF as shown in Table II [33,40–42]. Linear $U_s - u_p$ models (where U_s is the shock velocity and u_p is the particle velocity) were obtained from a least-squares fit to available published data for cerium where all data above 16 GPa were used for liquid Ce, and all data below 10 GPa were used for α-Ce. The resulting linear $U_s - u_p$ models were

TABLE I. Relevant experimental parameters and preliminary measured/calculated quantities.

Shot No.	V_p (km/s)	Imp. Mat.	L_{imp} (mm)	L_{Ce} (mm)	Particle Velocity u_p (km/s)	Long.[a] Stress P_x (GPa)	Estimated Temperature $T \times 10^3$ (K)	Hugoniot[b] Stress P_x^H (GPa)	Hugoniot Temperature $T^H \times 10^3$ (K)
1S1507	0.655 ± 0.001	Cu	6.033 ± 0.003	1.850 ± 0.003	0.451 ± 0.003	6.84 ± 0.01	0.757 ± 0.047	5.980 ± 0.01	0.737 ± 0.047
1S1488	0.842 ± 0.002	Al	5.999 ± 0.003	1.800 ± 0.003	0.435 ± 0.003	6.65 ± 0.01	0.612 ± 0.044	5.687 ± 0.01	0.595 ± 0.044
1S1474	0.797 ± 0.002	Cu	2.987 ± 0.003	1.500 ± 0.003	0.555 ± 0.011	8.70 ± 0.02	0.870 ± 0.106	7.870 ± 0.02	0.852 ± 0.106
1S1479	0.850 ± 0.002	Cu	2.966 ± 0.003	1.520 ± 0.003	0.596 ± 0.002	9.43 ± 0.01	0.962 ± 0.071	8.676 ± 0.02	0.944 ± 0.071
1S1480	0.853 ± 0.002	Ta	2.390 ± 0.003	1.580 ± 0.003	0.669 ± 0.006	10.75 ± 0.02	1.088 ± 0.059	10.46 ± 0.02	1.074 ± 0.059
2S0819	1.573 ± 0.003	Al	2.000 ± 0.003	1.250 ± 0.003	0.806 ± 0.003	13.30 ± 0.02	$1.290^{+0.088}_{-0.044}$	13.40 ± 0.03	$1.297^{+0.088}_{-0.044}$
2S0820	1.639 ± 0.003	Al	2.000 ± 0.003	1.250 ± 0.003	0.838 ± 0.003	13.96 ± 0.02	$1.348^{+0.088}_{-0.054}$	14.15 ± 0.03	$1.358^{+0.088}_{-0.054}$
2S0732	1.823 ± 0.004	Al	2.022 ± 0.003	1.036 ± 0.003	0.922 ± 0.004	15.63 ± 0.02	$1.364^{+0.066}_{-0.021}$	16.31 ± 0.03	$1.382^{+0.066}_{-0.021}$
2S0731	1.992 ± 0.004	Al	2.018 ± 0.003	1.483 ± 0.003	1.004 ± 0.003	17.30 ± 0.03	1.547 ± 0.049	18.40 ± 0.04	1.577 ± 0.049
2S0714	2.207 ± 0.004	Al	2.038 ± 0.003	1.270 ± 0.003	1.114 ± 0.003	19.63 ± 0.03	1.854 ± 0.073	21.17 ± 0.04	1.902 ± 0.073
2S0597	2.222 ± 0.004	Al	5.966 ± 0.003	1.810 ± 0.003	1.123 ± 0.004	19.83 ± 0.03	1.990 ± 0.200	21.37 ± 0.05	2.043 ± 0.200
2S0585	2.251 ± 0.005	Al	6.013 ± 0.003	1.670 ± 0.003	1.149 ± 0.004	20.39 ± 0.03	1.910 ± 0.143	21.76 ± 0.05	1.962 ± 0.143
2S0598	2.385 ± 0.005	Al	5.966 ± 0.003	1.810 ± 0.003	1.212 ± 0.003	21.78 ± 0.03	1.993 ± 0.084	23.58 ± 0.05	2.055 ± 0.084
2S0715	2.423 ± 0.005	Al	2.031 ± 0.003	1.418 ± 0.003	1.215 ± 0.003	21.84 ± 0.03	2.080 ± 0.091	24.11 ± 0.05	2.147 ± 0.091
2S0586	2.489 ± 0.005	Al	5.984 ± 0.003	1.625 ± 0.003	1.272 ± 0.003	23.13 ± 0.03	$2.259^{+0.381}_{-0.200}$	25.03 ± 0.05	$2.336^{+0.381}_{-0.200}$
2S0611	2.724 ± 0.005	Al	6.004 ± 0.003	1.910 ± 0.003	1.388 ± 0.003	25.80 ± 0.04	$2.364^{+0.228}_{-0.216}$	28.44 ± 0.06	$2.459^{+0.228}_{-0.216}$
2S0612	2.900 ± 0.006	Al	6.004 ± 0.003	1.520 ± 0.003	1.481 ± 0.004	28.02 ± 0.04	$2.485^{+0.401}_{-0.386}$	31.09 ± 0.07	$2.594^{+0.401}_{-0.386}$

[a]Longitudinal stress at the Ce-LiF interface.

[b]Calculated Hugoniot stress state prior to reflection of the shock wave at the Ce-LiF interface.

$U_s = 1.6572u_p + 1.209$ (km/s) for liquid Ce, and $U_s = 1.992u_p + 0.825$ (km/s) for α-Ce. Note that standard error analysis was used to estimate the uncertainty in each quantity shown in Table I.

A main objective of this work was to determine the Hugoniot temperatures for cerium in the solid and liquid phases, but wave propagation and interface interactions complicate the experiment and analysis. As shown in Fig. 3, the measured particle velocity and the temperature represents a final state that occurs following interaction of the incoming shock wave (blue-dashed line) with the Ce-LiF interface. Because the relative Impedance between cerium, Z^{Ce}, and LiF, Z^{LIF}, changes with pressure (or longitudinal stress), the wave interactions at the window fall into three cases. The first case is when $Z^{Ce} < Z^{LIF}$ which results in a reflected shock wave that propagates back into the cerium sample (red-dashed line). The second case occurs when $Z^{Ce} > Z^{LIF}$ resulting in a release wave that propagates back into the cerium sample (black-solid line). The third case is when $Z^{Ce} = Z^{LIF}$ resulting in no wave reflection at the interface. These high-pressure states were accurately described using a wave propagation code that incorporated a

Mie-Gruneisen EOS (no temperature dependence) with appropriate materials models (see Table II). As observed in Fig. 4, these one-dimensional simulations provided an adequate description of the shock response that will account for the Impedance effects on the shock wave propagation. With knowledge of the mechanical state of the sample, the measured temperature and particle velocity (or stress) provided a way to calculate the temperature on Hugoniot for the incoming shock wave. It was assumed that an implementation of the Elkin EOS [43] provided a reasonable description of the internal energy state of cerium over the small deviations from the principle Hugoniot (shock-up or release states) as it captures much of the available thermodynamic data available. For case 1, the temperature was calculated by application of the energy jump condition (shock-up) whereas for case 2, it was assumed that the material released along an isentrope to the final state. Temperature values for the Hugoniot state are shown in column 10 (Table I). It is important to note that the EOS predicts that the isentrope has a relatively small $\Delta T/\Delta P$, which implies that most of ΔP is accounted for in the cold curve portion of the equation of state. This is why the pressure difference

TABLE II. Relevant parameters used for a linear $U_s - u_p = C_O + Su_p$ model for impactors and windows used in this work where Γ is the Gruniesen gamma.

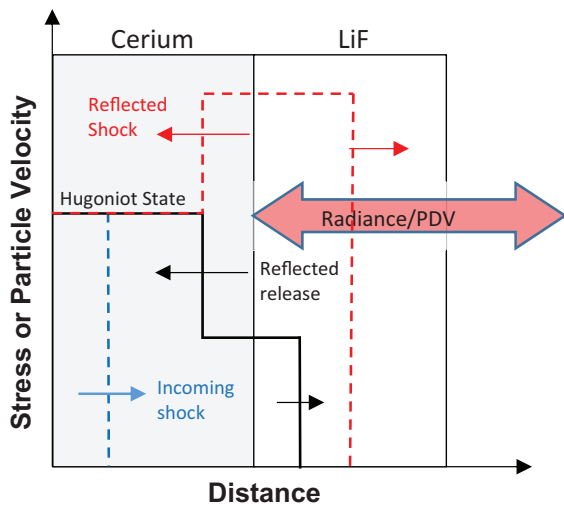| Material	Density	C_O	S	Γ
OFHC Cu	8.930	3.928	1.489	1.96
Al 6061-T6	2.703	5.288	1.3756	2.14
Ta	16.654	3.402	1.2196	1.8196
LiF	2.638	5.150	1.350	1.50

FIG. 3. Schematic showing the shock wave configuration. A shock wave is shown propagating toward the Ce-LiF interface, and then reflecting from the interface with two scenarios possible. For low impact velocities where the longitudinal stress is less than 13 GPa, the impedance of α-Ce is less than LiF resulting in a reflected shock wave to a higher stress state (red-dashed lines). For impact stresses greater than 13 GPa, the shock impedance of cerium exceeds that of LiF resulting in a release wave to a lower stress state (black lines). The red arrow indicates the radiance and PDV measurement monitoring the Ce-LiF interface.
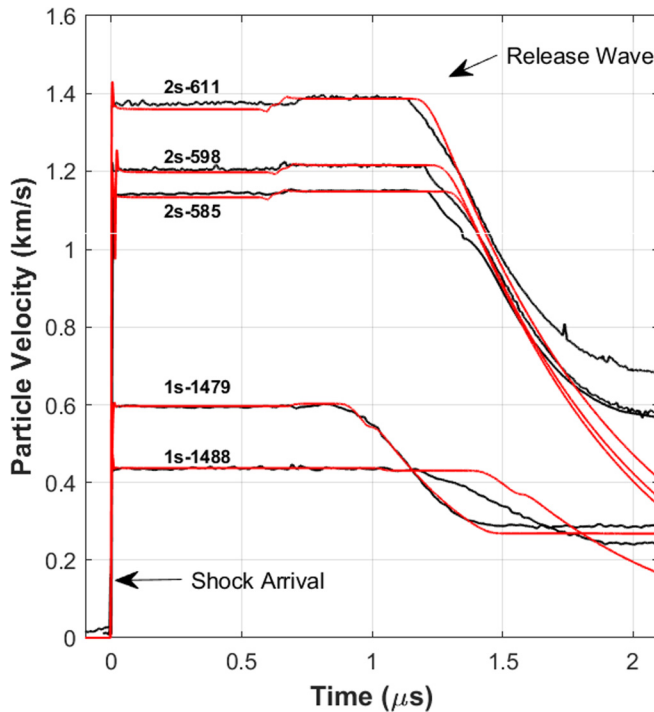
FIG. 4. Wave profile data for six experiments (black curves) along with calculated profiles (red curves) obtained using a one-dimensional hydrocode that used appropriate material models for the impactor and target materials. Note that differences in the release wave profile were observed because the model neglects strength effects and a nominal value of 1.5 was used for Gruneisen Γ.
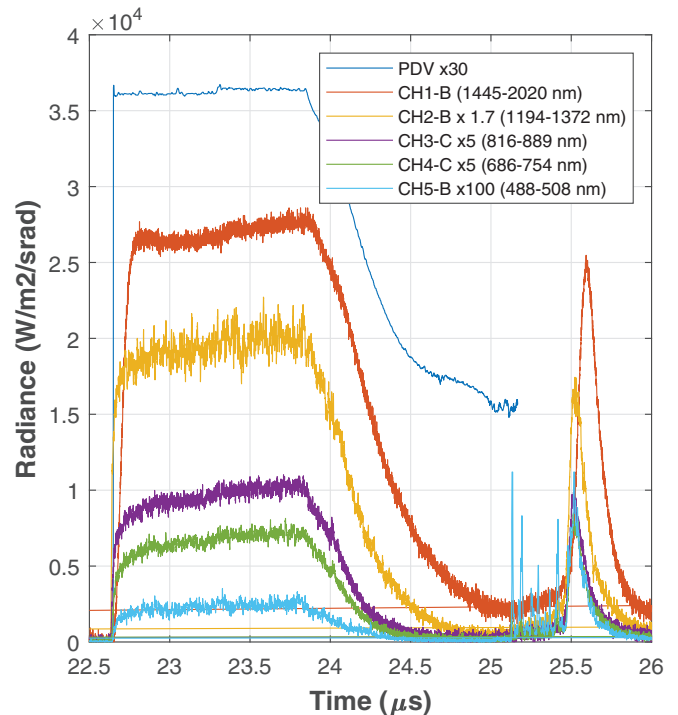

FIG. 5. Radiance data for five wavelengths plotted versus time for shot 2S-598. The particle velocity obtained from the PDV is plotted on the same time axis for comparison (scaled by $30\times$ arbitrarily). The data clearly show a significant increase in light at shock arrival up to a near steady state; it begins to decrease rapidly with the arrival of the release wave which takes the cerium to lower stress and temperature states.

between the measured and corrected stress values is greater than the measured and corrected temperature differences.

Wave profile data for six experiments are shown in Fig. 4 where the particle velocity (km/s) is plotted versus time (μs). All wave profiles show a sharp jump in particle velocity as the shock wave reaches the Ce-LiF interface followed by a steady state until the release wave arrives from the rear surface of the impactor. Calculated wave profiles obtained using the one-dimensional hydrocode, LASLO, show good agreement with the observed particle velocities in all experiments shown. Note that differences in the release wave profile were observed because the model neglects strength effects and a nominal value of 1.5 was used for Gruneisen Γ. Example radiance data for all channels (shot 2S-598) are plotted along with the PDV data for comparison in Fig. 5. The radiance data resemble the PDV data in shape with a sudden increase in observed light as the shock wave reached the Ce-LiF interface followed by a decrease in light as the release wave reaches the Ce-LiF interface. Remarkably, the profiles show little or no light prior to shock arrival indicating that the observed light was not caused by an impact flash, the hot gas pushing the projectile, or light generated during LiF fracture. Note that our analysis only considers the constant state achieved in the experiment, and additional work is required to analyze the radiance data during release.

An example of the calculated temperature profile for the shocked state obtained from the radiance data (Fig. 5), along
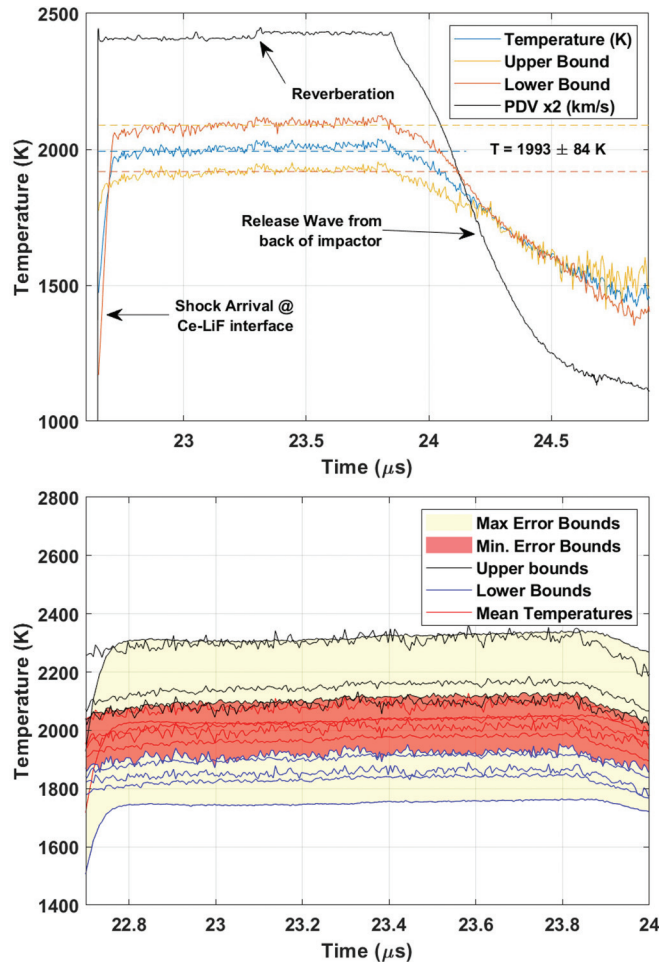
FIG. 6. Top: Average shocked temperature (blue curve) for Ce shot 2S-598 along with bounding temperatures. PDV data are plotted for comparison (arbitrarily scaled by 2×). Note the slight increase in temperature near $t = 23.3\ \mu$s which corresponds to a slight jump in particle velocity or stress caused by shock reverberation in the cerium sample. Bottom: Calculated temperatures from radiance data shown in Fig. 5. Average temperatures obtained from each channel are shown (red curves) along with all upper temperature bounds (black curves) and lower temperature bounds (blue curves). The shaded regions represent two estimates of the measurement uncertainty.

with the upper and lower bounds, is shown in Fig. 6 (top) where the temperature (in kelvins) is plotted versus time (μs) for shot 2S-598. The particle velocity profile is shown in the figure for comparison. Our analysis approach depended on the quality and consistency of the radiance data obtained in each experiment. For some experiments, the radiance data for all wavelengths proportionally tracked the particle velocity profile, backgrounds were controlled or eliminated, and all channels indicated similar apparent temperatures. In this case, bounding temperatures (upper and lower) were calculated for each wavelength assuming upper and lower bounds for the emissivity of 0.3 and 0.8, respectively. The average temperature was taken as the mean of these two bounds resulting in up to five temperature estimates per experiment for each wavelength as shown in detail in Fig. 6 (bottom). The temperature of the shocked state was taken as the average over

all five channels, and the uncertainty was taken as the nearest upper (blue curves) and lower bounds (black curves) as indicated by the red-shaded region. For the experiment shown, the steady-state temperature was $T = 1993 \pm 84$ K as shown in Fig. 6 (top). In some experiments, radiometry error (detector or recording malfunction, calibration error) or optical background (light from sample-window bond, anvil window flaw or edge release, gun drive impact flash, etc.) produced disagreement between temperatures calculated from the five channels of radiometry data. In these cases, the wavelengths (or channels) showing well-behaved radiances were used in the analysis to determine the average shocked temperature, and the error bounds were taken as the temperature bounds farthest from the average temperature as indicated by the yellow-shaded region in Fig. 6 (bottom).

IV. ANALYSIS AND DISCUSSION

Traditional sound speed measurements on shocked cerium point to an incipient shock melt transition near 10.2 GPa [29]. Thus, the T, P data in these two regions were analyzed to develop Hugoniot curves for α-Ce and liquid Ce separately, and to estimate the incipient and complete melting temperature and pressure. Finally, the data were compared to the predicted Hugoniot for both phases from a multiphase EOS and used to further constrain the model.

For solid α-Ce, the temperature-pressure data are summarized in Fig. 7 for stress states less than 11 GPa. The temperature (in kelvins) is plotted versus the longitudinal stress (GPa) with the measured values shown as red-filled triangles. As described previously, these values were corrected to account for the shock jump to higher stresses (caused by the higher impedance LiF window) resulting in the Hugoniot states shown as yellow-filled circles. The reported melt boundary [25] obtained using diamond cell methods is also shown for comparison. The data were fitted to a line and uncertainty bounds are shown as the red-shaded region which were calculated using a Monte Carlo, least-squares method. The incipient shock-melting temperature was taken as the value that corresponds to the Hugoniot state of 10.2 ± 0.34 GPa [29] resulting in a temperature of $T = 1051 \pm 89$ K (white-filled circle in Fig. 7). If we assume that incipient shock-melting occurs where the Hugoniot intersects the static melt boundary, then we arrive at slightly higher values of $T = 1130.2 \pm 24$ K and $P_x = 11.25 \pm 1.4$ GPa (blue-filled circle in Fig. 7). The former values are taken as the transition because sound speed measurements at pressure are still the most accurate way to determine incipient melting.

For liquid Ce, the temperature-pressure data are summarized in Fig. 8 for impact stresses greater than 11 GPa. The measured values for the temperature and pressure are shown (red-filled circles) along with the corrected values (yellow-filled circles) representing the Hugoniot states for each experiment. In contrast to the α-Ce data, the correction results in a shift to higher temperatures and stresses caused by a reflection of the shock wave to lower stress states at the LiF window. The temperature data exhibit an initial linear trend from 15 to 26 GPa with the two highest temperature experiments (2S-611 and 2S-612) deviating from linearity though the reason for this is uncertain. The data were fitted
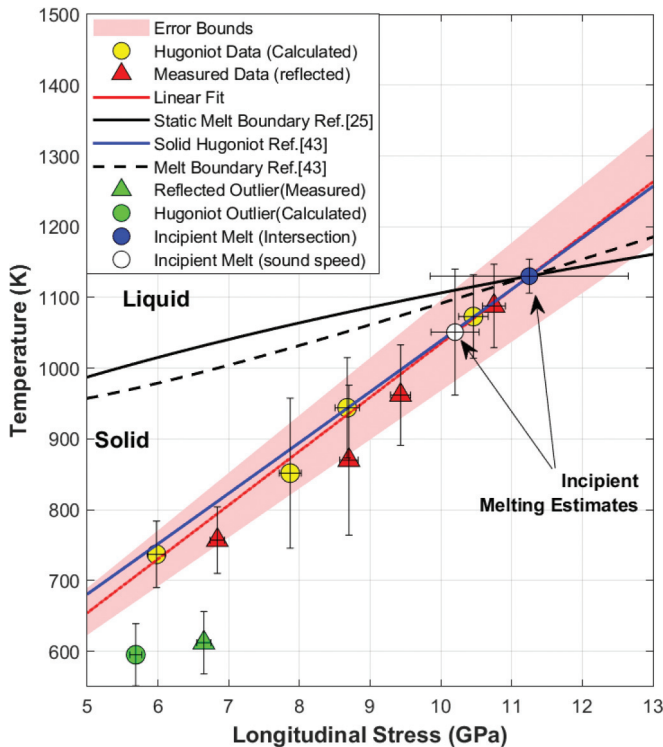
FIG. 7. Plot of temperature (K) vs longitudinal stress (GPa) for α-Ce ($P_x < 10$ GPa). A linear fit to the data results in the equation $T(P_x) = 76.18P_x + 273.2$. The green-filled data point represents an outlier that was not used in the fit. The incipient melt transition temperature was taken as the value that corresponded to the temperature at the incipient melt stress determined from previous sound speed measurements [29] (white-filled circle). Also shown is the temperature that corresponds to intersection of the measured Hugoniot with a published melt boundary (blue-filled circle) [25]. The solid-blue curve represents the solid Hugoniot obtained using the published multiphase EOS [43]. The red-shaded region indicates the estimated uncertainty in the fitted Hugoniot curve.
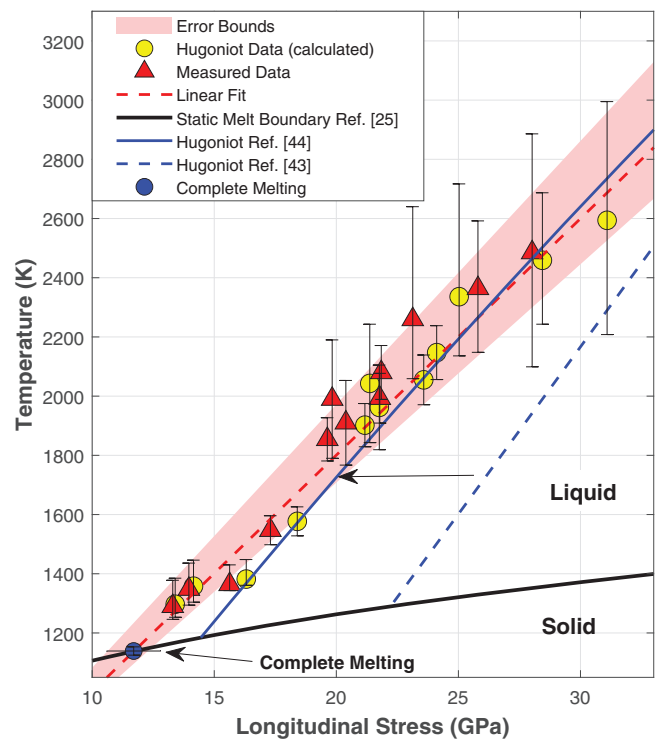

FIG. 8. Plot of temperature (K) vs longitudinal stress (GPa) for liquid Ce ($P_x > 10$ GPa). A linear fit to the data results in the equation $T(P_x) = 79.91P_x + 202.57$ K (red dashed line). The solid black curve represents the melt boundary obtained using the published multiphase EOS [43]. The modified Hugoniot curve [44] obtained from the multiphase EOS (blue curve) constrained using the T, P data from this work is shown along with the previous Hugoniot (blue-dashed line) constrained by earlier work [43]. The red-shaded region indicates the estimated uncertainty in the fitted Hugoniot curve.

to a line and complete melting was taken as the intersection of the linear fit with the static melt boundary. This resulted in an estimate for complete shock melting of $T = 1139 \pm 14$ K and $P_x = 11.7 \pm 1.1$ GPa. Note that in order to include the highest temperature data in a single fit, a second-order polynomial fit was required (not shown) which captures the nonlinearity observed at the highest temperatures.

To gain insight into the high-pressure response of cerium, the data were compared with calculations obtained using an available EOS [43] that was previously constrained using DAC data, thermal expansion data, and Hugoniot data. For the solid phase (Fig. 7), excellent agreement was observed between the experimental Hugoniot data (red curve) and the calculated curve (blue curve) whereas significant disagreement was observed for the liquid phase as shown in Fig. 8. This disagreement in the calculated and measured Hugoniot curves for liquid Ce largely originates from the lack of temperature data available to constrain the EOS and to accurately locate the completion of melt. The experimentally measured Hugoniots for the solid and liquid phases are summarized in Fig. 1 illustrating the significant change in the liquid Hugoniot location. To better constrain the EOS, a revised liquid

EOS parameter set was developed that was constrained using the temperature-pressure data obtained here. Following the formalism of Elkin [43] the two most influential parameters affecting temperature on the Hugoniot are the transition energy and the transition entropy although for this modified model all of the parameters were allowed to vary within physically reasonable ranges, and a least-squares fit was completed using a multivariable simplex method [44]. The parameters that changed most significantly were those found in the harmonic and anharmonic energy terms, or in other words, those that affect the temperature dependence of the internal energy. Comparison of the modified Hugoniot (solid-blue line) and the experimental data show improved agreement up to approximately 30 GPa.

V. CONCLUSIONS

Shock wave experiments were performed on cerium using pyrometry and interface velocimetry to determine the temperature and longitudinal stress for states that span the high-pressure α phase of cerium well into the liquid. The temperature data presented in this work provide an unprecedented mapping of the Hugoniot through the phase diagram while providing important constraints for understanding shock-induced melting for a metal. The experimentally determined

Hugoniot for α-Ce was in good agreement with an existing multiphase EOS for cerium and pointed toward a incipient melt transition of $T = 1051 \pm 89$ K for a transition stress $P_x = 10.2 \pm 0.34$ GPa. Complete shock melting was estimated to occur at $T = 1139 \pm 14$ K and $P_x = 11.7 \pm 1.1$ GPa. Comparison of the measured liquid Hugoniot with the EOS revealed differences including the location of complete melting. A revised EOS was developed by constraining the existing EOS with the temperature data obtained in this work showing improved agreement illustrating the importance of temperature data for understanding matter at extremes. It is important to note that additional refinements of the EOS are anticipated as we continue to explore other regions of the phase diagram. Work is underway to include recent data for the α-ϵ region [45] in the EOS, and to analyze release data to further constrain the liquid response.

[1] W. J. Carter, J. N. Fritz, S. P. Marsh, and R. G. McQueen, J. Phys. Chem. Solids **36**, 741 (1975).

[2] C. Dai, X. Jin, X. Zhou, J. Liu, and J. Hu, J. Phys. D **34**, 3064 (2001).

[3] D. Errandonea, B. Schwager, R. Ditz, C. Gessmann, R. Boehler, and M. Ross, Phys. Rev. B **63**, 132104 (2001).

[4] R. S. Hixson and J. N. Fritz, J. Appl. Phys. **71**, 1721 (1992).

[5] R. S. Hixson, D. A. Boness, J. W. Shaner, and J. A. Moriarty, Phys. Rev. Lett. **62**, 637 (1989).

[6] B. LaLone, G. Stevens, W. Turley, D. Holtkamp, A. Iverson, R. Hixson, and L. Veeser, J. Appl. Phys. **114**, 063506 (2013).

[7] B. LaLone, P. Asimov, O. Fat'yanov, R. Hixson, G. Stevens, and W. Turley, J. Appl. Phys. **126**, 225103 (2019).

[8] W. Turley, L. R. Veeser, M. D. Wilke, and J. A. Young, J. Appl. Phys. **110**, 103510 (2011).

[9] H. J. Kostkowski and R. D. Lee, *Theory and Methods of Optical Pyrometry* (US Department of Commerce, National Bureau of Standards, 1962).

[10] W. Nellis, F. H. Ree, R. Trainor, A. Mitchell, and M. Boslough, J. Chem. Phys. **80**, 2789 (1984).

[11] C. S. Yoo, N. C. Holmes, M. Ross, D. J. Webb, and C. Pike, Phys. Rev. Lett. **70**, 3931 (1993).

[12] N. C. Holmes, M. Ross, and W. J. Nellis, Phys. Rev. B **52**, 15835 (1995).

[13] D. Partouche-Sebban, D. Holtkamp, J. Pélissier, J. Taboury, and A. Rouyer, Shock Waves **11**, 385 (2002).

[14] D. Partouche-Sebban, J. Pelissier, W. Anderson, R. Hixson, and D. Holtkamp, Phys. B (Amsterdam) **364**, 1 (2005).

[15] J. Pelissier and D. Partouche-Sebban, Phys. B (Amsterdam) **364**, 14 (2005).

[16] A. Seifter and A. Obst, Int. J. Thermophys. **28**, 934 (2007).

[17] T. Ota, R. Amott, C. Carlson, D. Chapman, M. Collinson, R. Corrow, D. Eakins, T. Graves, T. Hartsfield, and D. Holtkamp, J. Dyn. Behav. Mater. **5**, 396 (2019).

[18] J. D. Bass, B. Svendsen, and T. J. Ahrens, in *High Pressure Research in Mineral Physics*, edited by M. Manghnani and Y. Syono (Terra Scientific, Tokyo, 1987).

[19] W. Nellis and C. Yoo, J. Geophys. Res. **95**, 21749 (1990).

[20] A. Schiwek, F. Porsch, and W. B. Holzapfel, High Pressure Res. **22**, 407 (2002).

[21] O. B. Tsiok and L. G. Khvostantsev, J. Exp. Theor. Phys. (Russia) **93**, 1245 (2001).

[22] G. Eliashberg and H. Capellmann, JETP Lett. **67**, 125 (1998).

[23] Ph. Schaufelberger, J. Appl. Phys. **47**, 2364 (1976).

[24] A. Jayaraman, Phys. Rev. **137**, A179 (1965).

[25] B. Sitaud, J. Pere, and Th. Thevenin, High Pressure Res. **12**, 175 (1994).

[26] M. J. Lipp, D. Jackson, H. Cynn, C. Aracne, W. J. Evans, and A. K. McMahan, Phys. Rev. Lett. **101**, 165703 (2008).

[27] B. J. Jensen and F. J. Cherne, J. Appl. Phys. **112**, 013515 (2012).

[28] G. N. Chesnut, W. W. Anderson, and J. Casson, in *Shock Compression of Condensed Matter 2006*, edited by M. D. Furnish, M. Elert, T. P. Russell, and C. T. White (American Institute of Physics, Baltimore, Maryland (USA), 2006), pp. 45–48.

[29] B. J. Jensen, F. J. Cherne, J. C. Cooley, M. V. Zhernokletov, and A. E. Kovalev, Phys. Rev. B **81**, 214109 (2010).

[30] O. T. Strand, L. V. Berzins, D. R. Goosman, W. W. Kuhlow, P. D. Sargis, and T. L. Whitworth Proc. SPIE **5580**, 593 (2004).

[31] B. J. Jensen, D. B. Holtkamp, P. A. Rigg, and D. H. Dolan, J. Appl. Phys. **101**, 013523 (2007).

[32] B. J. Jensen, D. B. Holtkamp, P. A. Rigg, and D. H. Dolan, J. Appl. Phys. **106**, 049901 (2009).

[33] R. Feng and Y. M. Gupta, Material models for sapphire, alpha-quartz, lithium fluoride, and fused silica for use in shock wave experiments and wave code calculations, Shock Dynamics Center Internal Report 96-XX, Washington State University, Pullman, WA, 1996.

[34] W. Turley, G. Stevens, G. Capelle, M. Grover, D. Holtkamp, B. LaLone, and L. Veeser, J. Appl. Phys. **113**, 133506 (2013).

[35] T. Hartsfield, B. La Lone, G. Stevens, L. Veeser, and D. Dolan, J. Appl. Phys. **128**, 015903 (2020).

[36] P. Herve, P. Masclet, A. Lefevre, and I. Gobin, in *Proceedings of the 4th Symposium on Temperature and Thermal Measurement in Industry and Science* (Finnish Society of Automatic Control, Helsinki, 1990), p. 315.

[37] E. Blanco and P. C. J. M. Mexmain, Shock Waves **9**, 209 (1999).

[38] E. D. Palik, *Handbook of Optical Constants of Solids*, Academic Press handbook series, Vol. 3 (Elsevier Science, 1998).

[39] A. C. Mitchell and W. J. Nellis, J. Appl. Phys. **52**, 3363 (1983).

[40] R. Feng and Y. M. Gupta, Material model for 6061-T6 aluminum for use in shock wave experiments and calculations, Internal Report 94-01, Shock Dynamics Center, 1994.

[41] D. Hayes, R. S. Hixson, and R. G. McQueen, in *Shock Compression of Condensed Matter*, edited by M. D. Furnish, L. C. Chhabilidas, and R. S. Hixson (American Institute of Physics, Snowbird, Utah, 1999), pp. 483–488.

[42] S. Marsh, *LASL Shock Hugoniot Data* (University of California Press, Los Alamos, NM, 1980).

[43] V. M. Elkin, V. N. Mikhaylov, A. V. Petrovtsev, and F. J. Cherne, Phys. Rev. B **84**, 094120 (2011).

[44] F. J. Cherne, Los Alamos Laboratory Report No. LA-UR 20-27865, Los Alamos, NM, 2020.

[45] B. Jensen, F. Cherne, and N. Velisavljevic, J. Appl. Phys. **127**, 095901 (2020).